Supplement of Atmos. Chem. Phys., 22, 4539–4556, 2022
https://doi.org/10.5194/acp-22-4539-2022-supplement

Atmospheric Chemistry and Physics
Open Access

Supplement of

The formation and mitigation of nitrate pollution: comparison between urban and suburban environments

Suxia Yang et al.

Correspondence to: Bin Yuan (byuan@jnu.edu.cn) and Min Shao (mshao@pku.edu.cn)

*Correspondence to: Bin Yuan (byuan@jnu.edu.cn) and Min Shao (mshao@pku.edu.cn)

Section S1. Split model configuration

During the observation periods, the diurnal variations of planetary boundary layer (PBL) at the GIG and Heshan sites are shown in Fig.S1 (a, b), which are based on data from the website of NOAA Air Resource Laboratory (https://ready.arl.noaa.gov/READYamet.php). The PBL height decreased significantly at 17:00, which would decouple into nocturnal surface boundary layer (NBL) and residual layer (RL). Besides, O_3 and NO_x at the ground site and 488 m site of Canton Tower agreed well during the day (shown in Fig. 5 (a) ~ (c)), and started to show clear distinction from 17:00 LT, thus we define 17:00 LT as the sunset time. At that time, the box was initialized by the last condition of the daytime model, and was separated into NBL and RL boxes. As the average boundary layer height was 400 m and 1000 m in the nighttime and daytime respectively, the heights of NBL and RL were set to 400 m and 600 m (Fig.S1 (c)). Both nighttime boxes were simulated from 17:00 to the 06:00 LT the following morning, at which time the PBL height began to gradually increase. After 06:00 LT, we assumed RL and NBL layer began to mix as the NBL height linearly increased, instantaneously mixing once per hour until 10:00 LT, the mixing process was completed, and two boxes were combined as a whole box. The mixed layer height was set as 1000 m in the simulation of daytime from 10:00 to 17:00 LT.

In the nighttime at the GIG site, the trace gases of NO_2 and O_3, meteorological parameters RH and *T* in the RL box, were constrained by the measurements from the 488 m site at Canton Tower. Several arguments justify this approach. Firstly, the trace gases at the surface GIG site were comparable with the Canton ground site in Fig.5, especially during the nighttime; the mean concentration deviations for NO, NO_2 and O_3 between the GIG and Canton ground sites were 1.96%, 6.54% and 0.65%, respectively. In addition, given the short distance between locations, we expect the composition of the aloft RL layer at GIG site to be closely represented by the Canton 488 m site. The O_3 at the Canton 488 m site was higher than at the ground site, and relatively unaffected by surface NO emissions, which would promote the nighttime NO_3 - N_2O_5 chemistry. The temporal evolution of other species in the RL, such as NO and VOCs, were unconstrained, and thus calculated by the box model.

However, there was no measurement aloft available for the campaign at Heshan site. Therefore, all species observed at Heshan site at 17:00 LT are set as the initial inputs for the RL box to freely evolve over night. To test this setting, we performed a simulation experiment using observations at GIG and Canton Tower sites. In analog to the settings of Heshan site, the observations at 17:00 LT at the GIG site were used as the initial inputs of RL, and allowed the initial data to freely evolve at night, without the influence from surface emissions. As shown in Fig.S11, the simulated nighttime results of NO_2 and NO_x in the RL compared well with the observation at the 488 m site of Canton Tower, which showed good agreements. Simulated O_3 and Ox were lower than the observations at the 488 m site of Canton Tower, but were within the combined uncertainties. In addition, the simulated nitrate and nitrate production rate from N_2O_5 uptake with the observation at the GIG site and 488 m Canton Tower site as initial input were also compared in Fig.S11(e ~ f), showing good agreement. Thus, we adopted this simulation method to perform the simulations at the Heshan site.

The physical loss that parameterized as a first order dilution process was the same as the daytime simulation in both the NBL and RL. We did the sensitivity tests combined with the unconstrained OVOCs species (MVK+MACR), O_3, HNO_3 and nitrate at the GIG and Heshan site, as shown in Fig.S2 and Fig.S3. A dilution rate of 24 h^{-1} for all species was determined at the GIG site, due to the good consistency between the simulation and observation for the chosen species. Comparing with the diurnal average observation, the simulated diurnal data had relative minor deviation with the observation by dilution constant of 8 h^{-1}. The average variations were -19% for MVK + MACR, -10% for O_3, 25% for HNO_3, and 12% for nitrate with the dilution constant of 8 h^{-1} at the Heshan site. Thus, the dilution constant of 24 h^{-1} and 8 h^{-1} were used at the GIG and Heshan site, respectively.

In addition to this dilution loss, the dry deposition rate for HNO_3 and O_3 were treated as first-order loss reactions in the model, set as 2.7 and 0.42 cm s^{-1} in the daytime, 0.88 and 0.14 cm s^{-1} in the nighttime NBL, as the deposition rate is known to decrease after sunset (Zhang et al., 2003;Womack et al., 2019).

Section S2 Thermodynamic ISORROPIAII model description

The presence of HNO_3 and NH_3 are conductive to form ammonium nitrate, which influenced by the aerosol pH and partitioning process of nitrate (Guo et al., 2018;Nenes et al., 2020). Thus, the thermodynamic ISORROPIA II model (Fountoukis and Nenes, 2007) was used to evaluate the NH_3 and sulfate impacts on the gas-particle partitioning process of nitrate. The model is run in the "forward" and "metastable" mode, which is used to calculate the gas-particle equilibrium concentrations. The model is based on the available input of total gas and particulate measured matter (HNO_3 + nitrate, NH_3 + ammonium, sulfate, and chloride), T and RH. The low concentration of nonvolatile cations (such as sodium, calcium, potassium, magnesium) in the PRD region is assumed to have minor impact on the thermodynamic equilibrium in PM_1 (Franchin et al., 2018;Guo et al., 2018).

Section S3 Calculation of nitrate production

The different mechanisms that increased nitrate concentrations in the simulations included three contributions: the reaction of OH and NO_2, heterogenous N_2O_5 uptake to the ground in the NBL, and nitrate mixed to the ground from the RL in the morning. The first two contributions were calculated by Eq. S (1) and Eq. S (2), combined with the R1 and R5 listed in the main text, which represented the nitrate production rate in surface boundary layer. The OH, N_2O_5 were based on the model results. $k_{[OH][NO_2]}$ was from the website of MCMv3.3.1 (https://mcm.york.ac.uk/).

$$P_{OH+NO_2} = k_{[OH][NO_2]}[OH][NO_2] * F \quad \text{S(1)}$$

$$P_{NBL(N_2O_5\ uptake)} = \frac{\omega 1 * \gamma * Sa}{4}[N_2O_5](2-\varphi) * F \quad \text{S(2)}$$

The production rate of OH + NO_2 in the model is the total HNO_3 production rate. The nitrate production rate from N_2O_5 uptake in the NBL is based on S (2), here F represents the partition ratio between HNO_3 and nitrate, which is calculated by Cp/ (Cp + Cg), where Cp and Cg are the observed concentration of nitrate and HNO_3, respectively.

With the convective growth of the planetary boundary layer (PBL) following sunrise, the polluted species in RL are vertically entrained into the NBL, which changes

surface pollutant concentrations (Curci et al., 2015;Chen et al., 2020). We assume the entrainment mixing process occurred from 6:00 to 10:00 (shown in Fig.S1 (c)), when the height of PBL (H_{PBL}) increased from 400 m to 1000 m, on the contrary, the height of RL (H_{RL}) linearly decreased from 600 m to 0 m, the nitrate produced from NBL and RL would participate in this process. The instantaneous mixed nitrate concentration (C_{mixed}) was the sum of nitrate mixed from RL (C_{RL}) and NBL (C_{NBL}), and the nitrate enhancement from the mixing process (P_{mixed}) was calculated by the difference of mixed nitrate concentration and the NBL nitrate concentration (C_{NBL}), which was described as follows:

$$C_{mixed,i} = C_{RL,i} \times \frac{H_{RL,i-1} - H_{RL,i}}{H_{PBL,i}} + C_{NBL,i} \times \frac{H_{PBL,i-1}}{H_{PBL,i}} \quad \text{S (3)}$$

$$P_{mixed,i} = C_{mixed,i} - C_{NBL,i} \quad \text{S (4)}$$

here *i and i-1* represent the current and previous time step, the changing height of different layers represent the weight coefficient of mixed nitrate concentration in RL and NBL. The hourly surface nitrate production was the sum of P_{OH+NO2}, $P_{NBL(N_2O_5\ uptake)}$ and $P_{mixed,}$ the total nitrate production in one day included the integral production of P_{OH+NO2} in the daytime (7:00 to 17:00 LT), $P_{NBL(N_2O_5\ uptake)}$ in the nighttime (from 17:00 to 6:00 LT the following morning), and P_{mixed} from 6:00 to 10:00 LT in the morning.

Section S4 Sensitivity test of isopleth diagrams from F0AM box model simulations.

In addition to the discussions about model simulation, several parameters used in the box model might influence the simulation results, which include the concentrations of HONO, the N_2O_5 uptake coefficient (γ) and the $ClNO_2$ yield (φ) (Lammel and Cape, 1996). Due to the uncertainty of HONO source and limited measurements, previous studies used the ratio between HONO and NO_x to constrain HONO, such as 0.8% in the high density traffic period in urban areas (Kurtenbach et al., 2001), 2% in the global chemical transport model (Elshorbany et al., 2012;Tan et al., 2019). In this study, we used the observed HONO as the base case, and ran the model in different sensitivity scenarios: with 0.8% of NO_x, with 2% of NO_x and with 2% of NO_2 as HONO concentrations (Fig. S13). Despite the different concentrations of HONO used in the

simulation, they all showed similar variation patterns for ozone and nitrate, indicating little influence of the HONO concentration parameterization on the simulation results. The γ and φ changed widely between laboratory and field studies (Mozurkewich and Calvert, 1988;Riedel et al., 2014;Wang et al., 2017;Yun et al., 2018;McDuffie et al., 2018). The parameterized γ and φ by updated empirical method by Yu et al. (2020) was applied in the base model. Here we chose the median value of γ (0.018) and φ (0.18) as the base input parameters; thus, different values of γ and φ were selected to perform sensitivity simulation (Fig. S14). Compared with the base case, the sensitivity of nitrate did not change with different values of γ and φ although the peak values of nitrate showed little differences with the changing of γ and φ. Overall, varying HONO, the N_2O_5 uptake coefficient, and the $ClNO_2$ yield would not be expected to change the sensitivity region of ozone and nitrate.

Table S1. Measured chemical species and the analytical methods, time resolution, limit of detection, the accuracy of the instruments used for different measured species, and sampling period at the GIG site.

chemical species	methods	time resolution	limit of detection	accuracy	sampling period
NMHC	GC-FID-MS	1 h	10 ~ 84 ppt	0.65% ~ 9.14%	2018.09.14~2018.11.19
Formaldehyde	PTR-TOF-MS	1 min	20 ppt	11.80%	2018.09.12~2018.11.19
Acetaldehyde	PTR-TOF-MS	1 min	33 ppt	12.50%	2018.09.12~2018.11.19
MVK+MACR	PTR-TOF-MS	1min	8 ppt	5.8%	2018.09.12~2018.11.19
HNO_3	TOF-CIMS	1 min	< 10 ppt	± 20%	2018.10.07~2018.11.19
N_2O_5	TOF-CIMS	1 min	< 10 ppt	± 25%	2018.10.07~2018.11.19
$ClNO_2$	TOF-CIMS	1 min	< 10 ppt	± 25%	2018.10.07~2018.11.19
NH_3	CRDS	1 min	1.0 ppb	± 35%	2018.09.30~2018.10.29
HONO	LOPAP	1 min	6.0 ppt	± 20%	2018.09.28~2018.11.19
O_3	UV absorption	1 min	0.5 ppb	± 10%	2018.09.11~2018.11.20
$NO/NO_2/NO_x$	Chemiluminescence	1 min	0.4 ppb	± 10%	2018.09.11~2018.11.20
CO	Infrared absorption	1 min	0.04 ppm	± 10%	2018.09.11~2018.11.20
NO_3^-, SO_4^{2-}, NH_4^+	TOF-AMS	300 s	0.005~0.024 μg m^{-3}	± 20%	2018.09.29~2018.11.20
Sa	APS (500 nm to 20 μm), SMPS (10 to 650 nm)	300s	—	± 10%	2018.09.29~2018.11.20
Photolysis frequencies	Spectrometer	10 s	—	± 10%	2018.09.18~2018.11.19

Table S2. Measured chemical species and the analytical methods, time resolution, limit of detection, the accuracy of the instruments used for different measured species, and sampling period at the Canton Tower site.

Location	chemical species	methods	time resolution	limit of detection	accuracy	sampling period
Ground site and 488 m site	O_3	UV absorption	1 min	0.5 ppb	± 10%	2018.09.20~2018.11.20
	$NO/NO_2/NO_x$	Chemiluminescence	1 min	0.4 ppb	± 10%	2018.09.20~2018.11.20
	CO	Infrared absorption	1 min	0.04 ppm	± 10%	2018.09.20~2018.11.20

Table S3. Measured chemical species and the analytical methods, time resolution, limit of detection, the accuracy of the instruments used for different measured species, and sampling period at the Heshan site.

chemical species	methods	time resolution	limit of detection	accuracy	sampling period
NMHC	GC-FID-MS	1 h	0.01 ~ 0.41 ppb	_	2019.09.25~2019.11.16
Formaldehyde	PTR-TOF-MS	1 min	29 ppt	15.6%	2019.10.16~2019.11.16
Acetaldehyde	PTR-TOF-MS	1 min	18 ppt	4.2%	2019.10.16~2019.11.16
MVK+MACR	PTR-TOF-MS	1min	7.3 ppt	5%	2019.10.16~2019.11.16
HNO_3	TOF-CIMS	1 min	< 10 ppt	± 20%	2019.10.01~2019.11.16
N_2O_5	TOF-CIMS	1 min	< 10 ppt	± 25%	2019.10.01~2019.11.16
$ClNO_2$	TOF-CIMS	1 min	< 10 ppt	± 25%	2019.10.01~2019.11.16
NH_3	GAC	30 mins	0.08 ppb	_	2019.09.25~2019.11.16
HONO	GAC	30 mins	0.1 ppb	_	2019.09.25~2019.11.16
O_3	UV absorption	1 min	0.5 ppb	± 10%	2019.09.25~2019.11.16
NO/NO_2/NOx	Chemiluminescence	1 min	0.4 ppb	± 10%	2019.09.25~2019.11.16
CO	Infrared absorption	1 min	0.04 ppm	± 10%	2019.09.25~2019.11.16
NO_3^-, SO_4^{2-}, NH_4^+	TOF-AMS	300 s	0.005~0.024 μg m^{-3}	± 20%	2019.10.02~2019.11.16
Sa	APS (500 nm to 20 μm), SMPS (10 to 650 nm)	300s	—	± 10%	2019.10.02~2019.11.16
Photolysis frequencies	Spectrometer	10 s	—	± 10%	2019.09.28~2019.11.16

178 **Table S4.** The mean volumetric concentrations of VOCs detected at the GIG and Heshan sites (Units: ppb)

Site	GIG	Heshan		GIG	Heshan
Species	Average ± SD		Species	Average ± SD	
Ethane	3.71±1.24	3.18±0.71	n-Heptane	0.11±0.15	0.24±0.23
Ethene	1.78±1.05	1.77±0.98	2-Methylheptane	0.02±0.02	0.13±0.2
Propane	6.88±5.1	4.22±1.85	3-Methylheptane	0.02±0.02	0.14±0.21
Propene	0.4±0.41	0.28±0.18	Toluene	2.02±1.9	3.44±1.65
i-Butane	1.76±1.32	1.64±0.8	n-Octane	0.05±0.05	0.25±0.18
n-Butane	3.15±2.46	3.17±1.67	Ethylbenzene	0.32±0.32	1.04±0.65
Acetylene	1.93±0.74	2.25±0.78	m/p-Xylene	0.91±0.87	4.01±2.22
trans-2-Butene	0.03±0.03	0±0.01	Nonane	0.04±0.03	0.24±0.07
1-Butene	0.08±0.05	0.05±0.04	o-Xylene	0.33±0.33	1.38±0.88
cis-2-Butene	0.02±0.02	_	Styrene	0.13±0.22	0.44±0.57
i-Pentane	1.33±1.06	2.38±2.6	Isopropylbenzene	0.01±0.01	0.1±0.1
n-Pentane	0.76±0.68	2.37±3.65	n-Propylbenzene	0.01±0.01	0.11±0.06
1-Pentene	0.03±0.02	0.01±0.01	m-Ethyltoluene	0.03±0.03	0.14±0.06
trans-2-Pentene	0.01±0.02	0±0.01	p-Ethyltoluene	0.02±0.02	0.15±0.07
Isoprene	0.14±0.15	0.14±0.19	n-Decane	0.02±0.02	0.06±0.02
cis-2-Pentene	0.01±0.01	0±0.01	1,3,5-Trimethylbenzene	0.02±0.02	0.13±0.04
2,2-Dimethylbutane	0.04±0.03	0.04±0.02	o-Ethyltoluene	0.02±0.01	0.1±0.03
2,3-Dimethylbutane	0.06±0.05	0.53±0.31	1,2,4-Trimethylbenzene	0.06±0.07	0.1±0.05
1-Hexene	0.02±0.01	0.02±0.06	1,2,3-Trimethylbenzene	0.02±0.01	0.06±0.02
n-Hexane	0.58±0.83	0.41±0.27	n-Undecane	0.01±0.01	_
2-Methylhexane	0.11±0.14	0.31±0.24	n-Dodecane	0.06±0.04	_
3-Methylhexane	0.13±0.18	0.32±0.25	Formaldehyde	2.53±1.62	2.42±1.2
Benzene	0.46±0.17	0.58±0.2	Acetaldehyde	1.95±1.2	3.14±1.64

179

180 **Table S5** Box model scenarios performed at the GIG and Heshan site

Site	Scenarios	Description about simulation	Other information
GIG	base case (S0)	set lifetime as 24 h, without N_2O_5 constrained	NBL: with observation at the GIG site; RL: with Observation at the 488m site of Canton Tower
	S1	set lifetime as 24 h, with N_2O_5 constrained	
Heshan	base case (S0)	set lifetime as 8 h, without N_2O_5 constrained	NBL: with observation at the Heshan site; RL: with observation at the Heshan site freely evolved
	S1	set lifetime as 8 h, with N_2O_5 constrained	

181

182

Table S6. The concentrations of chemical components (average ± standard deviation) and meteorological parameters during the investigated periods at the GIG and Heshan sites

Site	GIG	Heshan
PM_1 (μg m^{-3})	41.7±23.1	40.6 ±15.5
Organic (μg m^{-3})	16.9±9.0	21.6 ± 9.0
SO_4^{2-} (μg m^{-3})	10.1±4.6	6.9 ± 1.8
NO_3^- (μg m^{-3})	6.1±5.8	3.9 ± 3.0
NH_4^+ (μg m^{-3})	5.0±3.0	3.5 ± 1.5
Cl^- (μg m^{-3})	0.6±0.54	0.8 ± 1.3
BC (μg m^{-3})	3.2±1.1	4.0 ± 1.6
WS (m/s)	1.9±0.9	1.6±0.7
RH (%)	76.2±14.9	59.5±14.3
T(°C)	23.0±2.6	23.2±3.2

189 **Table S7**. Box Model performance for nitrate at the GIG and Heshan site

Site	Species	Observed	Modeled	MB[a]	RMSE[b]	IOA[c]	r[d]
GIG	Nitrate ($\mu g\ m^{-3}$)	6.2	7.4	1.2	4.9	0.84	0.77
Heshan	Nitrate ($\mu g\ m^{-3}$)	3.9	4.4	0.5	3.3	0.71	0.59

190 [a]: mean bias (MB), here we define the Obs_i and Mod_i as the observed and modeled
191 values at time i, respectively, and N represents the number of observations.

192 $$\mathrm{MB} = \frac{\sum(Mod_i - Obs_i)}{N}$$

193 [b]: root mean square error (RMSE);

194 $$\mathrm{RMSE} = \sqrt{\frac{1}{N}(\sum_{i=1}^{N}(Mod_i - Obs_i)^2)}$$

195 [c]: index of agreement (IOA), Obs_{aver} and Mod_{aver} represent the average
196 concentration of observation and model, respectively.

197 $$\mathrm{IOA} = 1 - \frac{\sum_{i=1}^{N}(Obs_i - Mod_i)^2}{\sum_{i=1}^{N}(|Obs_i - Obs_{aver}| + |Mod_i - Mod_{aver}|)^2}$$

198 [d]: the Pearson's correlation (r)

199

200 **Table S8.** OH radical production reactions included in the model simulation

201

Source	Reactions
Primary Source	HONO photolysis
	$O^1D + H_2O$
	H_2O_2 photolysis
	VOCs + O_3
ROx propagation cycle	HO_2 + NO

202

203

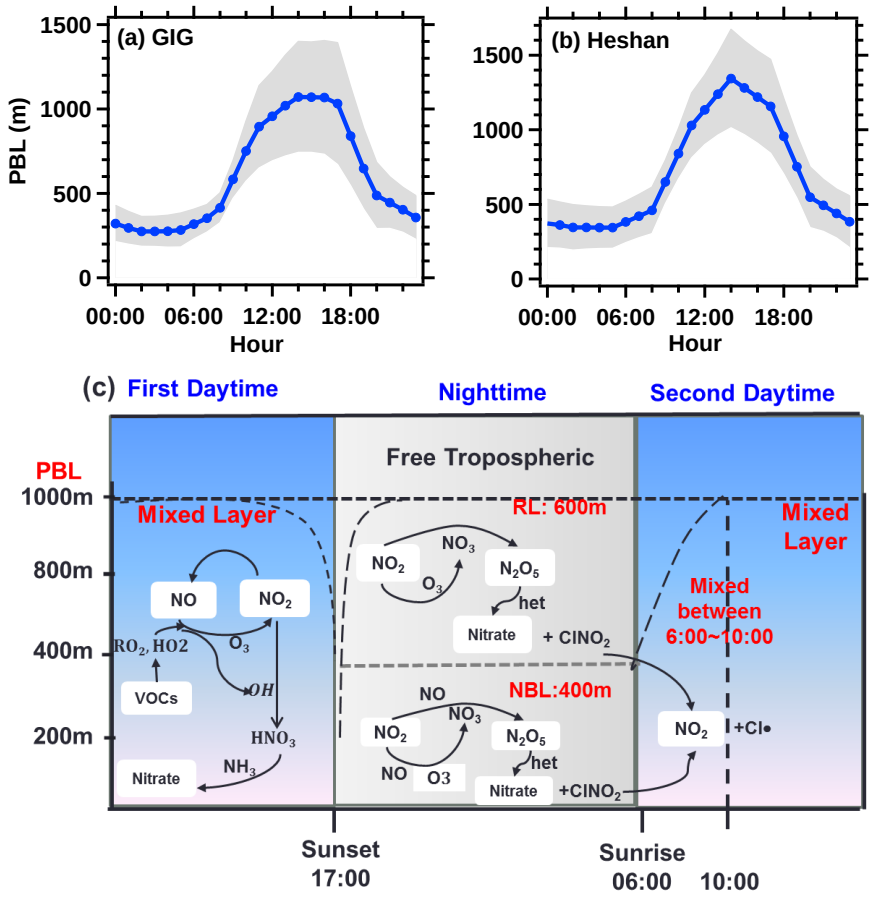

Figure S1. Diurnal variations of mean Planetary Boundary Layer (PBL) heights at (a) GIG site and (b) Heshan site, which were obtained from the NOAA Air Resource Laboratory website (https://ready.arl.noaa.gov/READYamet.php); (c) Schematic of PBL evolution and chemistry in the box model.

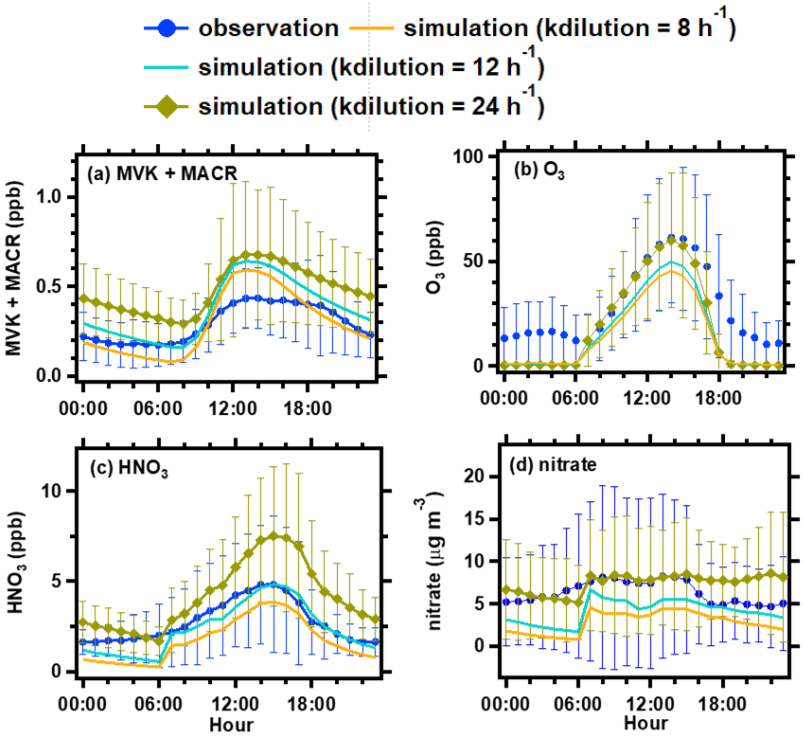

Figure.S2 Sensitivity tests with different dilution constant (kdilution) at the GIG site by box model.

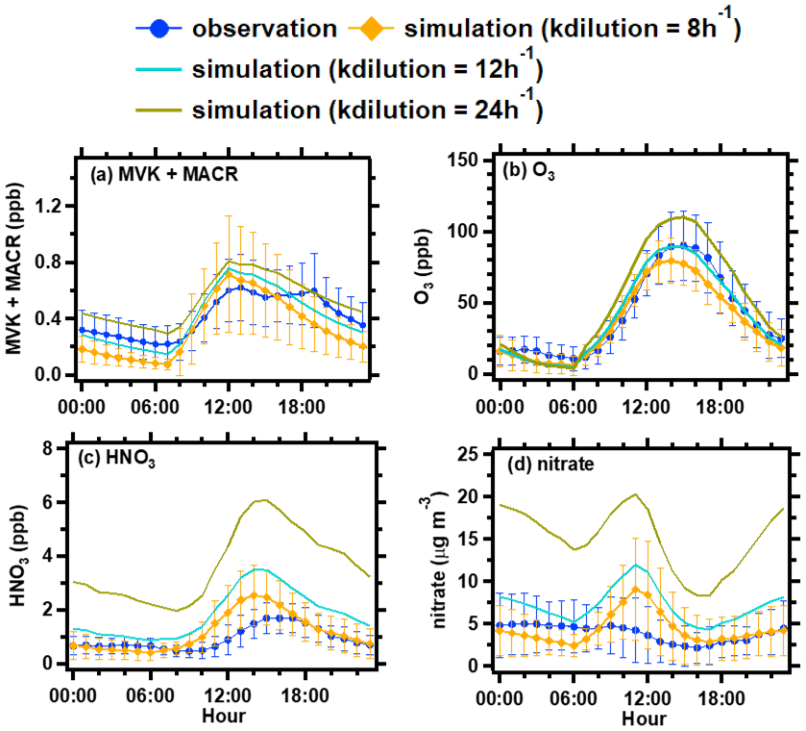

Figure.S3 Sensitivity tests with different dilution constant (kdilution) at the Heshan site by box model.

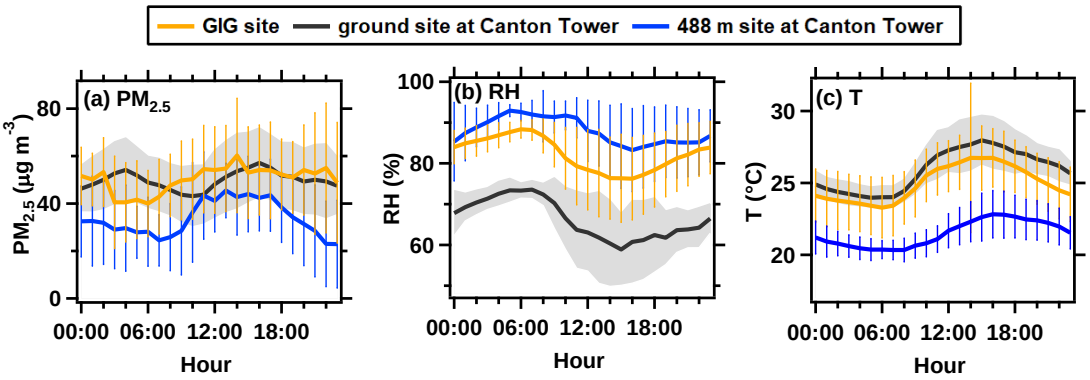

220

221 **Figure S4.** Diurnal variation of mean concentrations of (a) $PM_{2.5}$, (b) RH and (c) T at
222 GIG, ground site and 488m site of Canton Tower. The orange lines represent the
223 measurements at GIG site, and the blue and black lines represent the measurements at
224 488 m and ground site of Canton Tower, respectively. The orange and blue error bars
225 represent the standard deviations of the mean concentrations at GIG site and 488m site
226 of Canton Tower, and the grey areas show one standard deviation of the mean
227 concentration at ground site of Canton Tower.

228
229
230
231

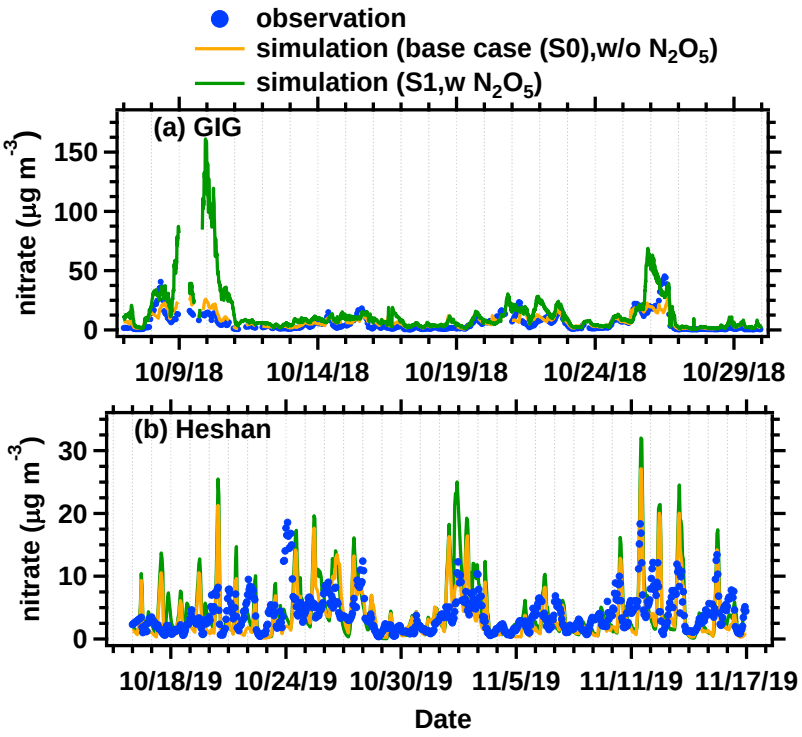

Figure S5. Comparison of the box model simulated and observed nitrate concentrations at (a) GIG site and (b) Heshan site. The orange lines represent simulated results of the base case (S0) without N_2O_5 constrained, and green lines represent the simulated results with N_2O_5 constrained (S1).

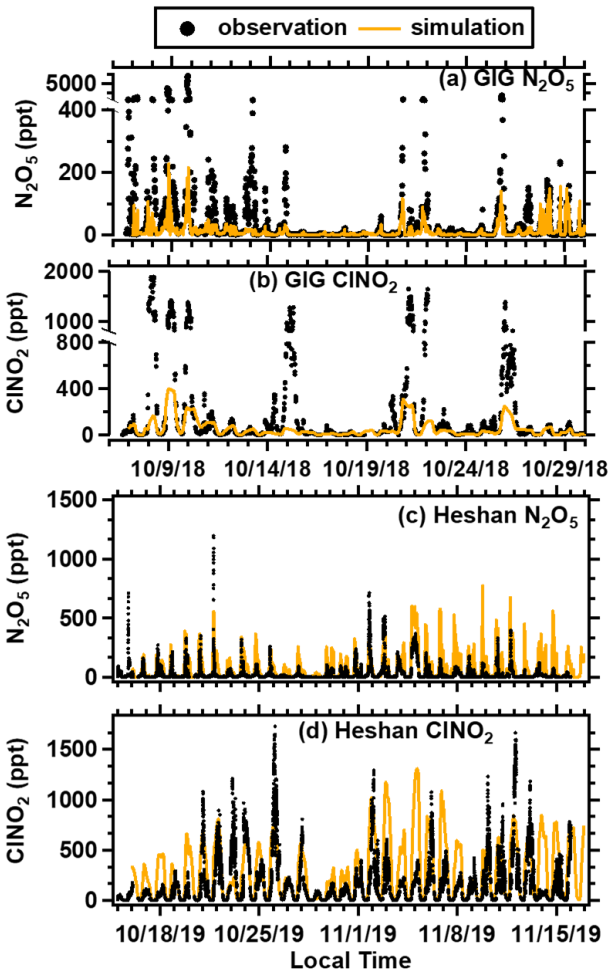

239

240 **Figure S6**. Comparison of the box model simulated and observed N_2O_5 and $ClNO_2$

241 concentrations at (a, b) GIG site and (c, d) Heshan site.

242

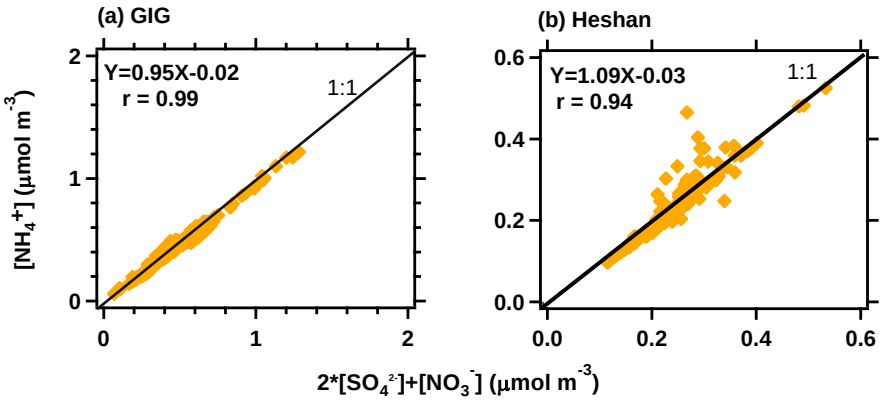

Figure S7. Scatter plot of $[NH_4^+]$ molar concentration versus $2*[SO_4^{2-}] + [NO_3^-]$ at the (a) GIG site and (b) Heshan site.

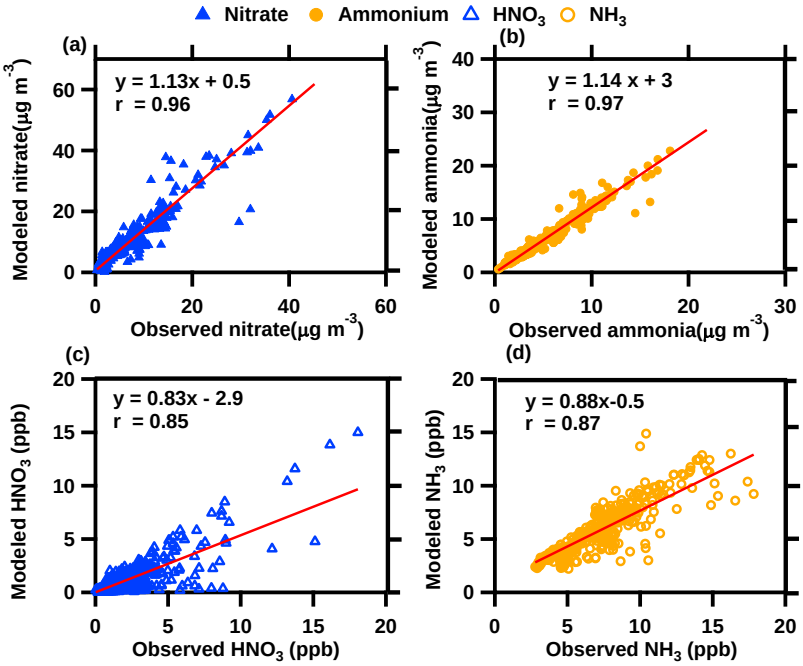

Figure S8. Scatter plot of observations vs ISORROPIA II modeled results of nitrate, ammonium, HNO_3 and NH_3 at the GIG site during the study period.

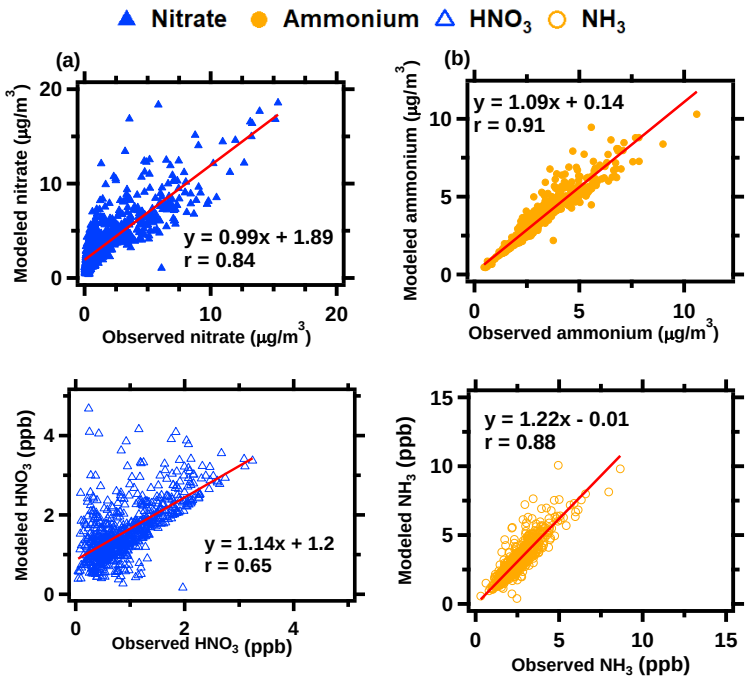

Figure S9. Scatter plot of observations vs ISORROPIAII modeled results of nitrate, ammonium, HNO_3 and NH_3 at the Heshan site during the study period.

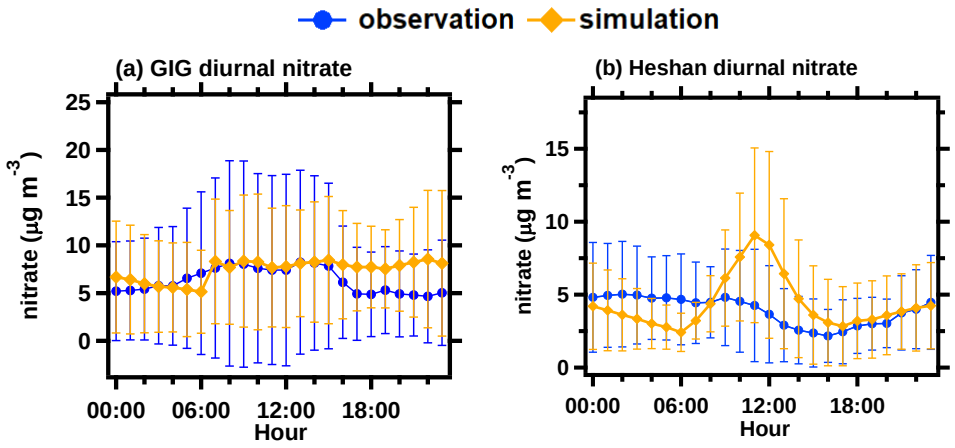

Figure S10. Comparison of daily-averaged box model simulated and observed nitrate at the GIG and Heshan site.

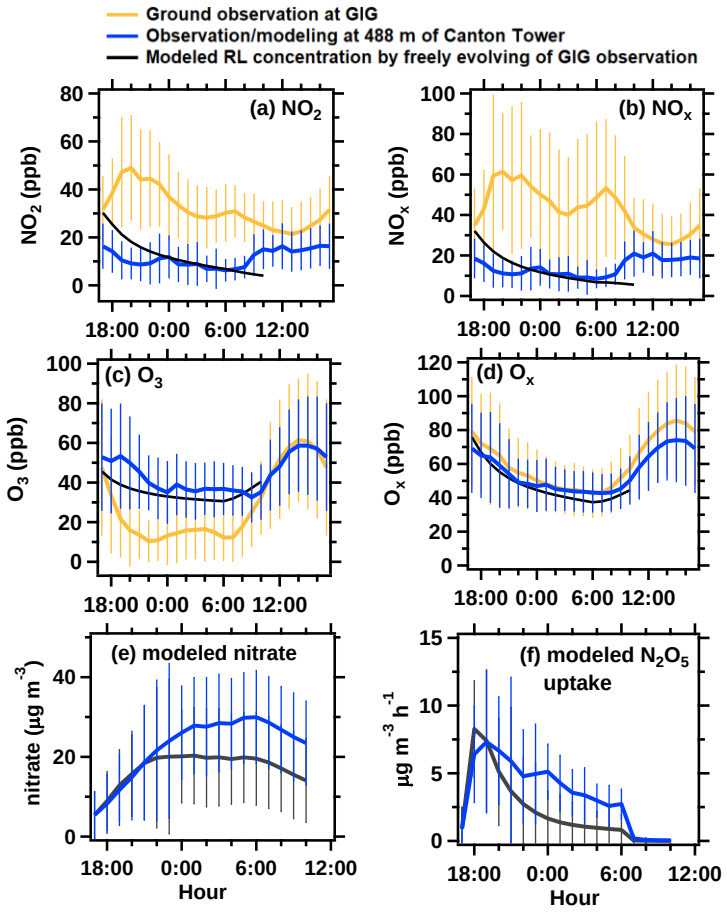

Figure S11. Time series of the simulated trace gases ((a) NO_2, (b) NO_x, (c) O_3 and (d) O_x) in the RL, when the observations at 17:00 LT at GIG were setting as the initial inputs of the RL simulation and all chemical species were freely evolved in the box model. (e) the simulated nitrate and (f) nitrate production rate from N_2O_5 uptake with the observation data at the GIG (black line) and 488m Canton Tower (blue line) as the initial inputs in the RL. The observations at GIG and 488m site of Canton Tower are also shown for comparison. The error bars represent the standard deviation of the observations.

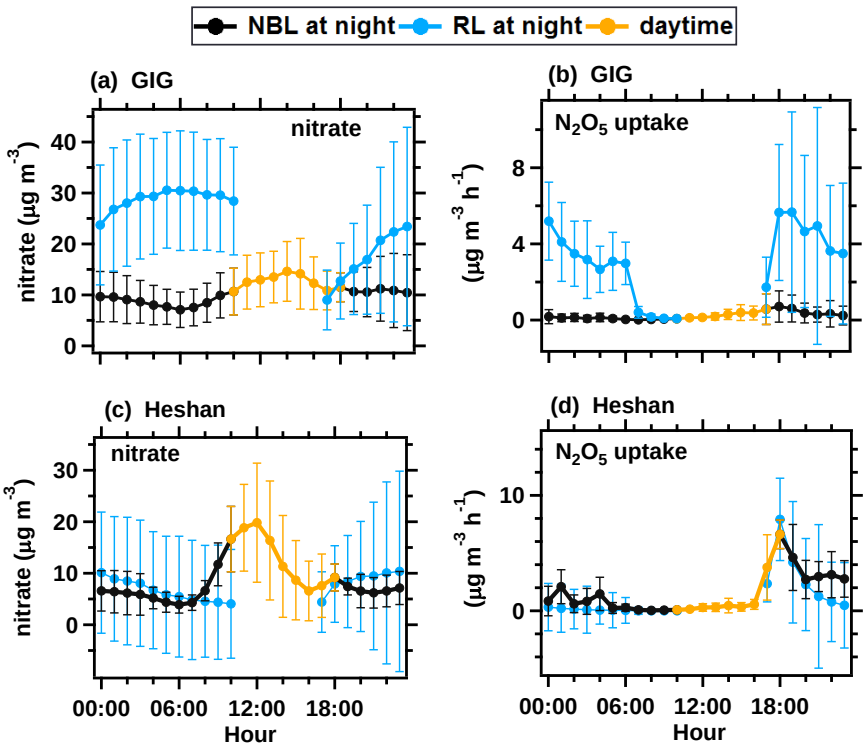

275

276 **Figure S12.** Comparison of the daily-averaged simulated nitrate concentration and

277 production rate from N_2O_5 uptake in the NBL and RL at the (a, b) GIG site and (c, d)

278 Heshan site**.** The error bars represent the standard deviation of the average data.

279

280

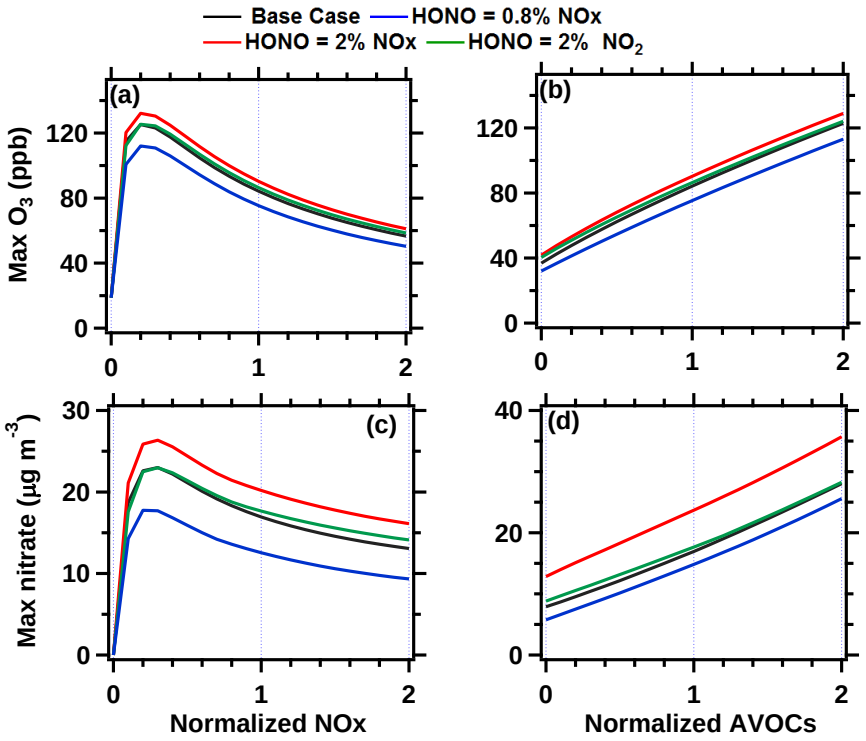

Figure S13. Sensitivity tests of HONO parameterization on the production of (a, b) ozone and (c, d) nitrate as a function of the normalized NOx and AVOCs relative to the base concentration at the GIG site.

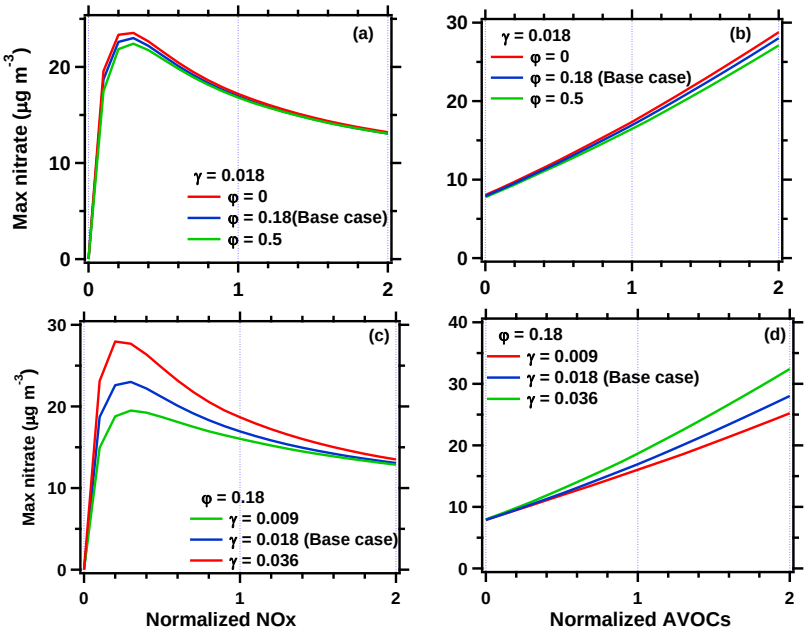

Figure S14. Sensitivity tests of the production yield of $ClNO_2$ (φ value) and the uptake parameter of N_2O_5 (γ value) on maximum nitrate concentrations as a function of the normalized NOx and AVOCs relative to the base concentration at the GIG site.

Reference

Chen, X., Wang, H., Lu, K., Li, C., Zhai, T., Tan, Z., Ma, X., Yang, X., Liu, Y., Chen, S., Dong, H., Li, X., Wu, Z., Hu, M., Zeng, L., and Zhang, Y.: Field Determination of Nitrate Formation Pathway in Winter Beijing, Environmental Science & Technology, 54, 9243-9253, https: //10.1021/acs.est.0c00972, 2020.

Curci, G., Ferrero, L., Tuccella, P., Barnaba, F., Angelini, F., Bolzacchini, E., Carbone, C., Der Gon, H. A. C. D. V., Facchini, M. C., and Gobbi, G. P.: How much is particulate matter near the ground influenced by upper-level processes within and above the PBL? A summertime case study in Milan (Italy) evidences the distinctive role of nitrate, Atmospheric Chemistry and Physics, 15, 2629-2649, https: //doi:10.5194/acp-15-2629-2015, 2015.

Elshorbany, Y. F., Steil, B., Brühl, C., and Lelieveld, J.: Impact of HONO on global atmospheric chemistry calculated with an empirical parameterization in the EMAC model, Atmospheric Chemistry and Physics, 12, 9977-10000, https://doi:10.5194/acp-12-9977-2012, 2012.

Fountoukis, C., and Nenes, A.: ISORROPIA II: a computationally efficient thermodynamic equilibrium model for K+–Ca2+–Mg2+–NH4+ –Na+–SO42− – NO3- –Cl−–H2O aerosols aerosols, Atmos. Chem. Phys., 7, 4639-4659, https: //10.5194/acp-7-4639-2007, 2007.

Franchin, A., Fibiger, D. L., Goldberger, L., McDuffie, E. E., Moravek, A., Womack, C. C., Crosman, E. T., Docherty, K. S., Dube, W. P., Hoch, S. W., Lee, B. H., Long, R., Murphy, J. G., Thornton, J. A., Brown, S. S., Baasandorj, M., and Middlebrook, A. M.: Airborne and ground-based observations of ammonium-nitrate-dominated aerosols in a shallow boundary layer during intense winter pollution episodes in northern Utah, Atmos. Chem. Phys., 18, 17259-17276, 10.5194/acp-18-17259-2018, 2018.

Guo, H., Otjes, R., Schlag, P., Kiendler-Scharr, A., Nenes, A., and Weber, R. J.: Effectiveness of ammonia reduction on control of fine particle nitrate, Atmos. Chem. Phys., 18, 12241-12256, https: //10.5194/acp-18-12241-2018, 2018.

Kurtenbach, R., Becker, K. H., Gomes, J. A. G., Kleffmann, J., Lörzer, J. C., Spittler, M., Wiesen, P., Ackermann, R., Geyer, A., and Platt, U.: Investigations of emissions and heterogeneous formation of HONO in a road traffic tunnel, Atmospheric Environment, 35, 3385-3394, https://doi.org/10.1016/S1352-2310(01)00138-8, 2001.

Lammel, G., and Cape, J. N.: Nitrous acid and nitrite in the atmosphere, Chemical Society Reviews, 25, 361-369, 10.1039/CS9962500361, 1996.

McDuffie, E. E., Fibiger, D. L., Dubé, W. P., Lopez-Hilfiker, F., Lee, B. H., Thornton, J. A., Shah, V., Jaeglé, L., Guo, H., Weber, R. J., Michael Reeves, J., Weinheimer, A. J., Schroder, J. C., Campuzano-Jost, P., Jimenez, J. L., Dibb, J. E., Veres, P., Ebben, C., Sparks, T. L., Wooldridge, P. J., Cohen, R. C., Hornbrook, R. S., Apel, E. C., Campos, T., Hall, S. R., Ullmann, K., and Brown, S. S.: Heterogeneous N2O5 Uptake During Winter: Aircraft Measurements During the 2015 WINTER Campaign and Critical Evaluation of Current Parameterizations, Journal of Geophysical Research: Atmospheres, 123, 4345-4372, https: //10.1002/2018JD028336, 2018.

Mozurkewich, M., and Calvert, J. G.: Reaction probability of N2O5 on aqueous aerosols, Journal of Geophysical Research: Atmospheres, 93, 15889-15896, https:

//10.1029/JD093iD12p15889, 1988.
Nenes, A., Pandis, S. N., Weber, R. J., and Russell, A.: Aerosol pH and liquid water content determine when particulate matter is sensitive to ammonia and nitrate availability, Atmos. Chem. Phys., 20, 3249-3258, https: //10.5194/acp-20-3249-2020, 2020.
Riedel, T. P., Wolfe, G. M., Danas, K. T., Gilman, J. B., Kuster, W. C., Bon, D. M., Vlasenko, A., Li, S. M., Williams, E. J., Lerner, B. M., Veres, P. R., Roberts, J. M., Holloway, J. S., Lefer, B., Brown, S. S., and Thornton, J. A.: An MCM modeling study of nitryl chloride (ClNO2) impacts on oxidation, ozone production and nitrogen oxide partitioning in polluted continental outflow, Atmos. Chem. Phys., 14, 3789-3800, https: //10.5194/acp-14-3789-2014, 2014.
Tan, Z., Lu, K., Jiang, M., Su, R., Wang, H., Lou, S., Fu, Q., Zhai, C., Tan, Q., Yue, D., Chen, D., Wang, Z., Xie, S., Zeng, L., and Zhang, Y.: Daytime atmospheric oxidation capacity in four Chinese megacities during the photochemically polluted season: a case study based on box model simulation, Atmos. Chem. Phys., 19, 3493-3513, https: //10.5194/acp-19-3493-2019, 2019.
Wang, H., Lu, K., Chen, X., Zhu, Q., Chen, Q., Guo, S., Jiang, M., Li, X., Shang, D., Tan, Z., Wu, Y., Wu, Z., Zou, Q., Zheng, Y., Zeng, L., Zhu, T., Hu, M., and Zhang, Y.: High N2O5 Concentrations Observed in Urban Beijing: Implications of a Large Nitrate Formation Pathway, Environmental Science & Technology Letters, 4, 416-420, https: //10.1021/acs.estlett.7b00341, 2017.
Womack, C. C., McDuffie, E. E., Edwards, P. M., Bares, R., de Gouw, J. A., Docherty, K. S., Dubé, W. P., Fibiger, D. L., Franchin, A., Gilman, J. B., Goldberger, L., Lee, B. H., Lin, J. C., Long, R., Middlebrook, A. M., Millet, D. B., Moravek, A., Murphy, J. G., Quinn, P. K., Riedel, T. P., Roberts, J. M., Thornton, J. A., Valin, L. C., Veres, P. R., Whitehill, A. R., Wild, R. J., Warneke, C., Yuan, B., Baasandorj, M., and Brown, S. S.: An Odd Oxygen Framework for Wintertime Ammonium Nitrate Aerosol Pollution in Urban Areas: NOx and VOC Control as Mitigation Strategies, Geophysical Research Letters, 46, 4971-4979, https: //doi.org/10.1029/2019GL082028, 2019.
Yu, C., Wang, Z., Xia, M., Fu, X., Wang, W., Tham, Y. J., Chen, T., Zheng, P., Li, H., Shan, Y., Wang, X., Xue, L., Zhou, Y., Yue, D., Ou, Y., Gao, J., Lu, K., Brown, S. S., Zhang, Y., and Wang, T.: Heterogeneous N2O5 reactions on atmospheric aerosols at four Chinese sites: improving model representation of uptake parameters, Atmos. Chem. Phys., 20, 4367-4378, https: //10.5194/acp-20-4367-2020, 2020.
Yun, H., Wang, W., Wang, T., Xia, M., Yu, C., Wang, Z., Poon, S. C. N., Yue, D., and Zhou, Y.: Nitrate formation from heterogeneous uptake of dinitrogen pentoxide during a severe winter haze in southern China, Atmos. Chem. Phys., 18, 17515-17527, https: //10.5194/acp-18-17515-2018, 2018.
Zhang, L., Brook, J. R., and Vet, R.: A revised parameterization for gaseous dry deposition in air-quality models, Atmos. Chem. Phys., 3, 2067-2082, https: //10.5194/acp-3-2067-2003, 2003.